Practically applicable water oxidation electrodes from 3D-printed Ti6Al4V scaffolds with surface nanostructuration and iridium catalyst coating [☆]

André Hofer [a], Sebastian Wachter [b], Dirk Döhler [a], Armin Laube [c,d], Beatriz Sánchez Batalla [e,a], Zongwen Fu [b], Claudia Weidlich [e], Thorsten Struckmann [c], Carolin Körner [b,f], Julien Bachmann [*,a]

[a] Friedrich-Alexander University of Erlangen-Nürnberg (FAU), Department of Chemistry and Pharmacy, Chemistry of Thin Film Materials, IZNF / Cauerstr. 3, 91058 Erlangen, Germany
[b] Friedrich-Alexander University of Erlangen-Nürnberg (FAU), Department of Materials Science, Joint Institute of Advanced Materials and Processes, ZMP / Dr.-Mack-Str. 77, 90762 Fürth, Germany
[c] Hamburg University of Applied Sciences (HAW), Department of Mechanical Engineering and Production Management / Berliner Tor 21, Hamburg 20099, Germany
[d] Instituto de Tecnologa Qumica, Universitat Politecnica de Valencia-Consejo Superior de Investigaciones Cientificas / Avenida de los Naranjos s/n, 46022 Valencia, Spain
[e] DECHEMA Research Institute, Applied Electrochemistry / Theodor-Heuss-Allee 25, 60486 Frankfurt am Main, Germany
[f] Friedrich-Alexander University of Erlangen-Nürnberg (FAU), Department of Materials Science, Chair of Materials Science and Engineering for Metals (WTM) / Martensstrae 5, 91058 Erlangen, Germany

ARTICLE INFO

ABSTRACT

This study establishes the applicability of 3D printing (additive manufacturing) towards the generation of titanium alloy scaffolds for water oxidation electrodes. The scaffolds can be subsequently nanostructured by electrochemical anodization to enhance their surface area and coated with iridium as the electrocatalyst. We focus on the characterization of the functional electrodes in process-relevant conditions (1 M H_2SO_4, 60 °C, stirring) in terms of their performance and stability in a holistic manner. Various preparative conditions yield various patterns of performance and stability, as quantified by overpotentials η_{10} in steady-state electrolyses, maximum current densities j_{max} in dynamic voltammetry, surface roughness rf, and by overpotential increase, iridium loss, and j_{max} decrease after 100 h of operation, on the other hand. In other words, the system is highly flexible and can be adapted to specific constraints depending on the application chosen.

1. Introduction

Sustainable energy production being inherently intermittent, storage of electrical power represents the bottleneck towards a net-zero economy. One attractive storage option is the electrolysis of water [1,2].

A water electrolyzer is an electrochemical cell in which H_2O is split into oxygen at the anode and hydrogen at the cathode. Of these two half-reactions, the oxidation of water to oxygen (oxygen evolution reaction, OER) is the more challenging one, so that reducing the overpotential required for this half-reaction is most urgently needed to improve the overall device efficiency. The electrode scaffold, coated with the active catalyst, must be stable in the harsh operation conditions of function, namely concentrated acidic electrolyte (e.g. H_2SO_4) and elevated tem-

peratures. Anodes for such electrolyzers can be made out of titanium, due to its ability to form a passivation layer of TiO_2 in aqueous solutions. This oxide provides corrosion resistance at room temperature [3].

Titanium, worldwide one of the most abundant metals (approx. 0.6% of the earth's crust) [4] is a very commonly used material in the aerospace, automotive and food industry, power and petrochemical plants, in refineries, heat exchangers or marine structures due to its outstanding properties with a very high material's strength, corrosion resistance in ambient conditions (room temperature and non-fluorinated aqueous solutions), mechanical similarity to mild steel and high temperature stability [4]. The utilization of this non-noble metal in a variety of applications with diverging standards has led to the development of various purity grades and alloy compositions with properties

---

commensurate with the applications. Among those, Ti6Al4V is one of the most commonly used alloys of titanium not only in industry but also in medical prostheses [4,5], also known as Titanium grade 5 as classified by the American Society for Testing and Materials (ASTM). This particular alloy is also suited to additive manufacturing via electron beam processing approaches [6–9].

Although additive manufacturing (3D printing) has been applied in the electrochemical field in a number of cases, [10–15] the combination of electrode scaffolds generated by 3D printing with subsequent surface treatment for increase of the geometry area and noble metal catalyst coating has not been reported to date. In this paper, we eliminate this gap by combining additive manufacturing with chemical methods: we establish a preparative procedure that allows us to generate 3D-printed titanium-based electrodes featuring surface nanostructuring and catalyst coating. We characterize the structure, performance, and stability obtained with various experimental conditions. We demonstrate that the method is applicable to the generation of electrodes in original geometries, such as cylindrical ones as opposed to the planar plates and felts used traditionally. From there, the range of geometries achievable for electrolyzer electrodes is limited solely by the experimental constraints of electron beam processing and the experimentalist's imagination. Complex, three-dimensional geometries may be used to optimize fluid flow, surface area, and electrical characteristics with a broad freedom in a manner that is not possible with traditional (subtractive) methods of electrode manufacturing.

2. Results and discussion

2.1. Preparation and materials characterization

a. Preparation

The first step of our procedures consists of Ti6Al4V selective electron beam melting (SEBM), whereby the parameters are chosen so as to sinter the particles as opposed to melting them altogether [16]. This approach serves to generate a scaffold with some porosity on the scale of tens of microns (Fig. 1d). In the second step, we perform anodization, an electrochemical surface treatment that serves to increase surface area in a controlled manner via the formation of titanium dioxide nanotubes. This cost-effective, single-step technique allows one to tune the size and shape of the tubes by careful adjustment of the process parameters (electrolyte, potential, duration, temperature), [17–20] and thereby adjust the 'roughness factor' rf (defined as the ratio between microscopic and macroscopic geometric surface areas of the sample). It also provides some degree of corrosion resistance. In the third step, we use atomic

layer deposition (ALD) to load the noble metal catalyst, iridium, in minute amounts. The catalyst further contributes to chemical stability and corrosion resistance, depending on the loading. ALD is a chemical thin coating method based on self-limiting surface reactions from the gas phase, with the unique capability of generating conformal layers on geometrically complex substrates such as the deep pores used here [21–27]. It also provides outstanding control of the amounts deposited. Specifically, the Ir deposition method has been optimized and demonstrated for the OER in earlier work already [28–31]. The choice of metallic iridium as the catalyst is dictated by its outstanding electro-catalytical properties [32]. It is the standard (electro-) catalysts for the oxygen evolution reaction (OER) in proton exchange membrane water electrolytic cells. Although the utilization of Ir results in significant costs originating in the limited abundance of the noble metal, its good catalytic activity and equally important stability in harsh conditions have rendered it unavoidable in this field [33]. The anodization step was optimized for commercially available felts consisting of smooth, pure titanium fibers, [34] yet its applicability to the complex geometry and chemical composition of sintered Ti6Al4V has not been established.

Our characterization of the SEBM-printed Ti6Al4V electrodes by energy-dispersive X-ray microanalysis (EDX) and X-ray diffraction (XRD, Fig. 2 black) allows us to identify the expected composition of the alloy: Ti (88 at%) with smaller amounts of Al (9 at%) and V (4 at%). The alloy consists predominantly of the α-phase (hcp, empty circles in XRD), with minute amounts of the β phase (bcc, full disks).

In the next step, we perform anodization of these Ti6Al4V electrodes in various conditions and characterize the microscopic structures obtained. Subsequently, we will investigate how these structural parameters translate into performance and stability (in process-relevant conditions, namely 1 M H_2SO_4 and 60 °C) as quantified in a multiparameter, systematic analysis. The electrochemical anodization is performed in a purpose-built two-electrode cell in which the Ti6Al4V tubular working electrodes (125 mm length, 5 mm outer diameter, 0.5 mm wall thickness, ESI Figure S1) are sandwiched between two graphite counter-electrodes in order to generate a homogeneous electric field on the 3D surface. The large graphite plates provide at least 10 times larger surface area than the workpiece and yield similar results as an expensive platinum counter-electrode [17]. Two different organic and fluoride-containing electrolytes (based on glycerol and ethylene glycol, respectively) are tested and compared, which mainly differ in their viscosity and added water content. Organic electrolytes are preferred over aqueous ones for the generation of a highly self-organized nano-tubular layer, due to their inhibition of oxide dissolution on top of the pores, whereas the formation of a hexafluoro titanium complex
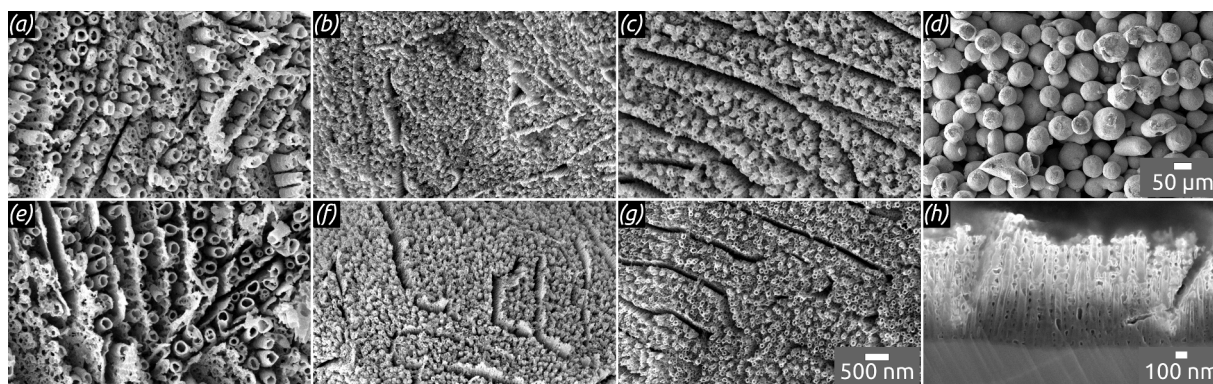

Fig. 1. Characterization of 3D printed Ti6Al4V electrodes (outer shell) obtained after anodization and Ir coating. Anodization is performed in ethylene glycol with 20% H_2O and 0.3 wt% NH_4F under 60 V for 3 h *(a)/(e)* and in glycerol-based electrolyte with 12% H_2O and 0.5 wt% NH_4F under 40 V for 2 h *(b)/(f)* or 4 h *(c)/(g)* duration. Subsequently, half of the electrodes were annealed at 450 °C for 4 h in order to chance TiO_2 into the anatase crystal structure *(e)/(f)/(g)*. Micrograph *(d)* shows the sintered Ti6Al4V powder particles at a lower magnification forming the tubular electrode and *(h)* shows the cross-section of the sample presented in *(c)/ (d)* featuring the titania tubes on every Ti6Al4V powder particle with a pore length of approx. 1 µm. A comparison of the resulting surface structuring of the inner and outer cylinder surfaces can be found in the supporting information, Fig. S1.
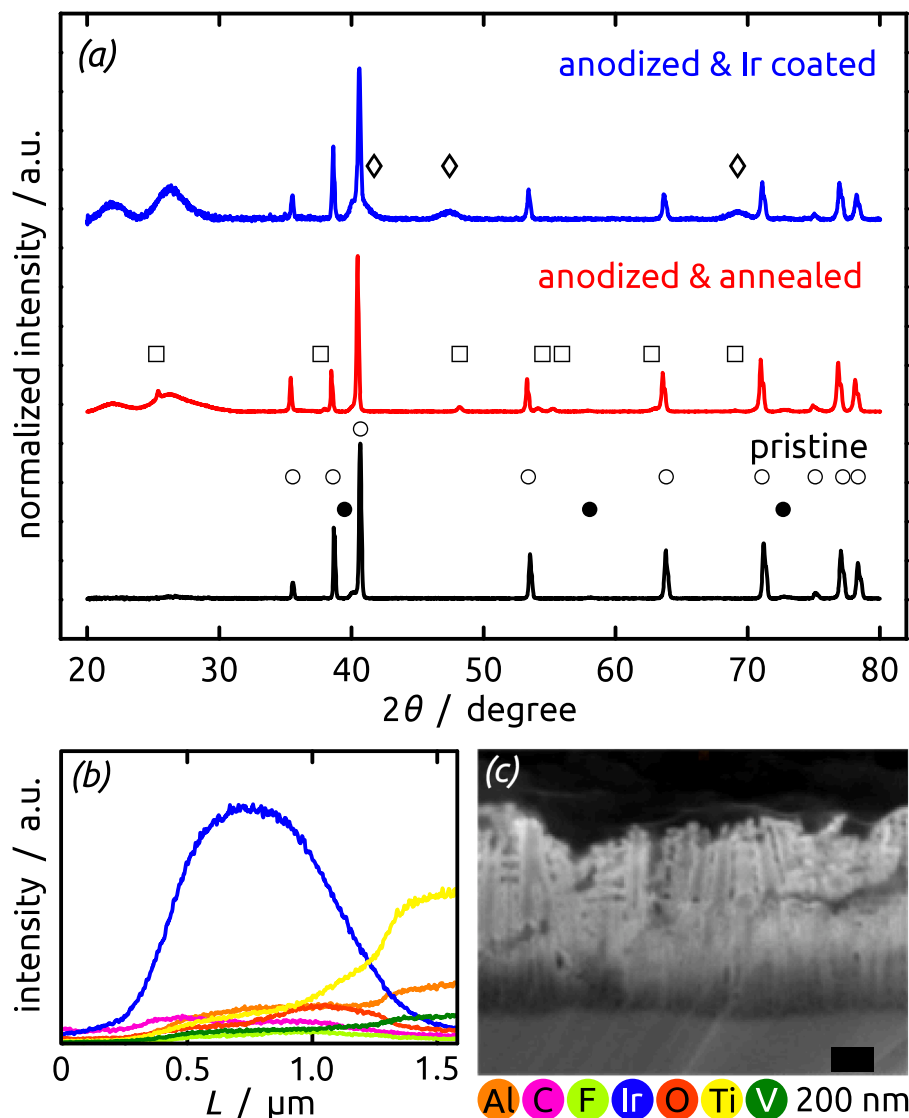
Fig. 2. *(a)* XRD pattern of Ti6Al4V electrode: pristine (black), obtained after 4 h anodization and subsequent annealing (red) as well as after anodization in glycerol with 12% H_2O and Ir coating (blue, Fig. 1–*(c)/(d)/(g)/ (h)*), showing ◊ nanocrystalline cubic Ir (COD9008470: 41°, 47°, 69°), □ TiO_2 in anatase modification (COD5000223: 25°, 38°, 48°, 54°, 55°, 63°, 69°), ∘ α Ti (hcp, COD1534878: 35°, 40°, 53°, 64°, 71°, 75°, 77°, 78°) and ● β Ti (bcc, COD9012924: 39°, 58°, 73°). Uniform coating of the TiO_2 tubes with metallic Ir is proven by the EDX line graph from the pores' top to the sintered particle bulk in *(b)* as well as *(c)* the SEM micrograph of the cross section combined with EDX mapping.

generates a chemically reactive site at the pore's extremity, allowing the tubes to grow into the metal particle [17,34]. The peculiar confined geometry of the tube-shape electrode and its large surface area require constantly pumping the electrolyte through the anodization cell in order to ensure efficient dissipation of the heat generated in the electrochemical process. The strongly corrosive electrolyte is circulated through a heat exchanger, the cool side of which is maintained at room temperature by a circulating chiller. The test conditions chosen for anodization based on preliminary work on pure titanium felts are: voltage 40 V for 2 h and 4 h in glycerol-based electrolyte (GLY, mixed with 0.5 wt.% NH_4F and 12 vol.% H_2O, higher viscosity), and 60 V for 3 h in ethylene glycol electrolyte (EG, with 0.3 wt% NH_4F and 20 vol.% H_2O, lower viscosity) [18].

b. Characterization

In XRD (Fig. 2a), anodized electrodes annealed to 450 °C (red curve) still exhibit predominantly the peaks associated with the metallic alloy, whereas the presence of titania is indicated by very weak peaks at 25°, 38°, 48° and 55° for anatase TiO_2 and the broad signals between 20° and 30° corresponding to amorphous titania. Microstructural characterization by scanning electron microscopy is best performed with a thin metallic, conductive layer, therefore we will present it after catalyst coating. This coating by ALD completes the electrode fabrication

procedure. It involves the alternating reactions of the surface with the ALD precursors (EtCp)Ir(CHD) and ozone, O_3, repeated 150 times to deposit a nominal thickness of 9 nm Ir [28–31,34]. We note that, as highlighted in the publications cited, nucleation inhibition leads to an actual loading with Ir that may be an order of magnitude lower than the nominal value determined on a planar reference.

The top-view scanning electron micrographs of the sample surfaces after anodization and ALD (Fig. 1) reveal that the pore inner diameter (Table 1) increases with increasing water content from 35 nm (*(b)* GLY, 12% H_2O, 2 h), to 60 nm (*(c)* GLY, 12% H_2O, 4 h) and to 170 nm (*(a)* EG,

Table 1
Titania tube inner diameter and electrical length specific resistance comparison of samples generated with different anodization electrolytes: NH_4F in glycerol (2 h/4 h) and ethylene glycol (3 h) and optionally annealed at 450 °C for 4 h.

sample	tube diameter nm	length specific resistance mΩ cm
pristine	n/a	2.1
EG, 3 h	170	2.2
EG, 3 h, a.	170	2.2
GLY, 2 h	35	2.2
GLY, 2 h, a.	35	2.5
GLY, 4 h	60	2.2
GLY, 4 h, a.	62	2.0

20% H_2O, 3 h) due a higher dissolution rate of titania. The more elevated potential applied for anodization in EG also has a significant contribution to the pore diameter obtained in this electrolyte [17,35]. This large pore diameter is expected to be deleterious for performance since it results in lower specific surface area. However, the comparison of Fig. 1b/c shows that increasing this surface area via long anodization durations (which yield long pores) also causes the formation of cracks (presented in cross-section in Fig. 1h), which likely result in poor corrosion resistance. Additionally, a comparison of cross-sections indicates that the long anodization durations do not correlate with longer pores. Instead, redissolution of TiO_2 simply causes larger inner pore diameters. In fact, all three anodization procedures result in tubes of approximately 1 μm length [17,35–38].

The presence of metallic Ir throughout the porous titania layer after ALD is demonstrated by XRD (41°, 47°, 69°: COD 9008470) [39,40] and EDX, Fig. 2b/c. Annealing the samples at 450 °C for 4 h under atmospheric oxygen in order to convert the amorphous titania to anatase does not significantly affect the pore diameter or length in this temperature range. However, it enhances the crack formation (Fig. 1e/f/g). Annealing does not significantly improve the overall electrical conductivity of the tubular scaffolds (Table 1). All six samples reach an overall conductivity of approximately $5 \cdot 10^4$ S m^{-1} for the macroscopically defined tubular shape. Given the highly porous (roughly 90% porous) structure, this corresponds to an intrinsic specific conductivity on the order of $0.2 \cdot 10^{-4}$ Ω m, which is about an order of magnitude lower than literature values for bulk Ti6Al4V (171–178 μΩ cm), [41,42] as expected based on the large density of sinter contacts.

c. Electrochemically active surface area (ECSA)

Determining the catalytically active surface area of an electrode remains a challenge in electrocatalysis. In the most reliable approach, the proton reductive adsorption capacity value Q_{ox}^H is determined by impedance spectroscopy (EIS) and compared with the known density $Q_{ox,ML,s}^H$ of hydrogen adatoms possible on a planar noble metal surface (surface coverage factor θ) to yield the electrocatalytically active area [43,44] at the adsorption potential. It is then converted to the roughness factor rf based on the macroscopic surface area A_{macro} of the sample [45].

$$rf = \frac{Q_{ox}^H}{\theta \cdot Q_{ox,ML,s}^H} \cdot A_{macro}^{-1} \qquad (1)$$

The values presented in Table 2 call for several comments. Firstly, the microscopic ECSA is at least two orders of magnitude larger than the area of a perfect cylinder of 5 mm diameter and 125 mm length. Secondly, annealing increases rf, in agreement with observations of enhanced surface roughness upon crystallization of the originally amorphous titania. Thirdly, the duration of anodization in GLY electrolyte is not reflected in rf. This is perfectly in line with the observation mentioned above that the tube length is similar for samples anodized for 2 h and 4 h. Here, EG and GLY electrolytes deliver similar values.

d. Corrosion

Titanium as the electrode scaffold material was chosen due to is excellent stability in harsh conditions (e.g. concentrated acids). However, titanium is not a noble metal and its high corrosion resistance in aqueous environments is caused by the immediately formation of a thin titanium dioxide film acting as passivation layer. The stability of the metal in corrosive conditions is fully reliant on the stability of the titania film, which has been intensively investigated in a broad variety of solvents, acids and bases, but predominantly at room temperature only [3]. In this study, we investigate the stability, performance and applicability of Ti6Al4V electrodes towards the OER in realistic conditions, that is, in sulfuric acid at pH 0 and 60 °C. The corrosion potential E_{corr} and corrosion current density j_{corr} were calculated (Table 3) using linear sweep voltammetry (LSV, scan rate 20 mV min^{-1}, Fig. 3). The pristine (as-printed) material inititially exhibits a rather high potential of $E_{corr} = -1.14$ V (vs. $E^{\circ}(H_2O)$) with a rather low $j_{corr} = 0.58$ mA cm^{-2}, due to passivation as mentioned. However, the finite solubility of TiO_2 in acids [3] at elevated temperatures causes a fast degradation. We observe that within several hours, E_{corr} shifts by several hundred mV cathodically, while j_{corr} increases by two orders of magnitude, before the electrode dissolves completely (supporting info).

Anodization of the alloy results in a slight reduction in j_{corr} but also a slightly more negative value of E_{corr}. Subsequent ALD of Ir has the opposite effect. The corrosion potential is significantly more positive, whereas the corrosion current determined initially is similar to that of the naked metal. The major difference is observed during long-term measurements (presented in Figure S2 of the Supporting Information). This time, maintaining the fully treated (anodized, coated) electrodes for several days (100 h) in the hot, concentrated electrolyte does not cause any measurable degradation. The j_{corr} value remains constant while E_{corr} shifts anodically.

2.2. Electrochemical performance

The LSV curves presented in Fig. 3, recorded on electrode segments of 1 cm length offer an obvious demonstration of catalytic activity by our Ir deposit when the extremity of the curves at $\eta = 0.5$ V is considered. The maximum current density j_{max} is two to three orders of magnitude larger with ALD-treated samples than with uncoated ones. The pristine (gray, a) and anodized Ti-alloy substrates without Ir-coating (dark green/blue/brown, b/c/d) exhibit no catalytic activity towards the OER at all. Among the ALD-coated ones (bright colors, e-j), the highest j_{max} values are achieved with the amorphous titania electrodes. Let us now perform a systematic quantification of the six different types of Ir-containing electrodes.

The performance of an electrochemical device can be quantified with various parameters. Here, we will consider three distinct quantifiers for water oxidation in application-near conditions, namely in 1 M H_2SO_4 at 60 °C and under stirring:

Table 2
Roughness factor (rf) of Ti6Al4V electrodes anodized in glycerol (40 V, 2 h or 4 h) and in ethylene glycol (60 V, 3 h) determined by EIS measurements of proton reductive adsorption after full electrocatalytic performance characterization.

H_2O	rf
EG, 3 h	300
EG, 3 h, a.	420
GLY, 2 h	300
GLY, 2 h, a.	420
GLY, 4 h	100
GLY, 4 h, a.	230

Table 3
Corrosion measurements of Ti6Al4V electrode scaffolds after various treatments: pristine, electrochemical anodized and iridium coated in sulfuric acid at pH 0 and 60 °C.

sample	potential E_{corr} vs. RHE / V	current density j_{corr} mA cm^{-2}
pristine	0.09 ± 0.12	0.58 ± 0.15
EG, 3 h, w/o Ir	0.02 ± 0.07	1.31 ± 0.57
GLY, 2 h, w/o Ir	0.02 ± 0.02	0.51 ± 0.31
GLY, 4 h, w/o Ir	0.02 ± 0.06	5.94 ± 3.20
EG, 3 h	0.50 ± 0.03	2.43 ± 1.37
EG, 3 h, a.	0.50 ± 0.04	8.76 ± 6.07
GLY, 2 h	0.44 ± 0.07	3.84 ± 0.58
GLY, 2 h, a.	0.49 ± 0.04	4.89 ± 1.05
GLY, 4 h	0.56 ± 0.03	1.35 ± 0.46
GLY, 4 h, a.	0.53 ± 0.05	4.42 ± 0.44

(a) overpotential broken down into activation and ohmic contributions extracted from a fit of the linear sweep voltammetry (LSV) curves;

(b) overpotential η_{10} needed to reach 10 mA cm^{-2} in steady-state electrolysis (chronoamperometric electrolysis measurements recorded for two hours at each potential) initially and later on for stability after approx. 100 h of electrochemical characterization;

(c) and a more dynamic value is furnished by the current density j_{max} achieved in cyclic voltammetry at the overpotential $\eta = 0.5$ V, complemented by charge transfer resistance R_{ct} determined from electrochemical impedance spectroscopy.

a. Overpotentials from full LSV curve fits

The overpotential η describes the potential beyond the thermodynamic potential of the H$_2$O/O$_2$ couple, $E' = 1.198$ V at 60°, needed to reach a certain current density. The analysis of the LSV curves presented in Fig. 3 and in Supporting Information allow one to extract three distinct contributions to the overall overpotential: (i) the activation energy of the electrochemical reaction itself (η_{act}), (ii) transport along a concentration gradient (convection, diffusion, migration: η_{conc}), and (iii) the ohmic losses within the bulk solid and liquid phases: [46–48]

$$E = E' + \eta_{act} + \eta_{ohm} + \eta_{conc} \tag{2}$$

The activation overpotential can be determined at any value of j from the logarithmic contribution to the curve, based on the Tafel equation, [47]

$$\eta(j) = \frac{RT}{\alpha n F} \cdot \ln \frac{j}{j_0} \tag{3}$$

with the gas constant R, temperature T, and exchange current density j_0. The ohmic overpotential combines effects by the ionic resistance of the electrolyte and the electric resistance of the entire external circuit, and it can be extracted based on the linear $\eta(j)$ behavior described by Ohm's Law [47]. transport and thus the concentration overpotential becomes the limiting factor at high current densities, and is found to not be significant in our system.

Figure 4 summarizes the activation and ohmic overpotential values determined for 10 mA cm^{-2} for all six samples. At this reasonably low current density, the ohmic contribution is lower than activation, and annealing tends to reduce η_{act} slightly. However, these small gains are more than compensated for by concomitant increases of η_{ohm}. This unexpected observation indicates that the conductivity increase obtained by crystallizing the originally amorphous titania is overcompensated by another effect. In other words, the main resistance is not caused by the anodic oxide layer but rather by the contact quality at the various interfaces within this system.

b. Steady-state electrolyses

Let us now consider the most practically relevant performance, namely the stabilized, steady-state one. Here, the electrode's overpotential for a given current density is the performance indicator commonly accepted as the most meaningful one. The values determined in steady-state chronoamperometric electrolyses (Fig. 5a) to reach 10 mA cm^{-2} are summarized in Table 4 ($\eta_{10,ini.}$). The pristine additively manufactured scaffold (gray curve in Fig. 5a) provides the background for an inactive structure. The best performance (lowest overpotential η_{10}) is obtained by anodizing the scaffolds in ethylene glycol under 60 V for 3 h (brown). However, the anodization conditions yield a minor effect when compared to annealing. All samples annealed before Ir ALD exhibit significantly lower performance than their counterparts with no thermal treatment, an observation that parallels the electrical transport measurements presented above.

c. CV current density and EIS

A more detailed analysis of electrode performance allowing one to distinguish between morphology and electrocatalytic influences is enabled by electrochemical impedance spectroscopy (EIS). Potentiostatic EIS measurements presented in Supporting Information allow one to distinguish the differences in specific surface area between samples. Double-layer capacity values C_{dl} mirror rf trends observed above. Charge transfer resistance R_{ct} values determined at $\eta = 0.4$ V are presented in Table 4. The R_{ct} of all amorphous electrodes are in the range of
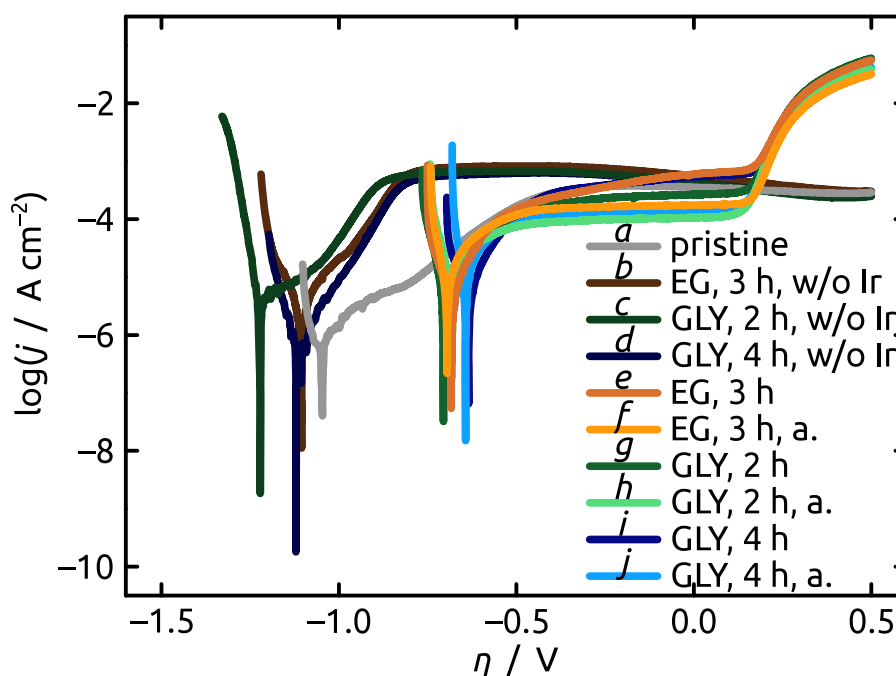

Fig. 3. Linear sweep voltammety (LSV, scan rate 20 mV min^{-1}) of Ti6Al4V electrodes anodized in glycerol (2 h/4 h) or ethylene glycol (3 h) electrolytes and subsequently Ir coated by ALD. Measurements were performed in 1 M H$_2$SO$_4$ at 60 °C using a three-electrode setup with a graphite auxiliary and (Hg/Hg$_2$SO$_4$/1 M H$_2$SO$_4$) reference electrode. The measurement presented is the best (highest current density at $\eta = 0.5$ V, corresponding 1.73 V vs. RHE) of three identical samples.
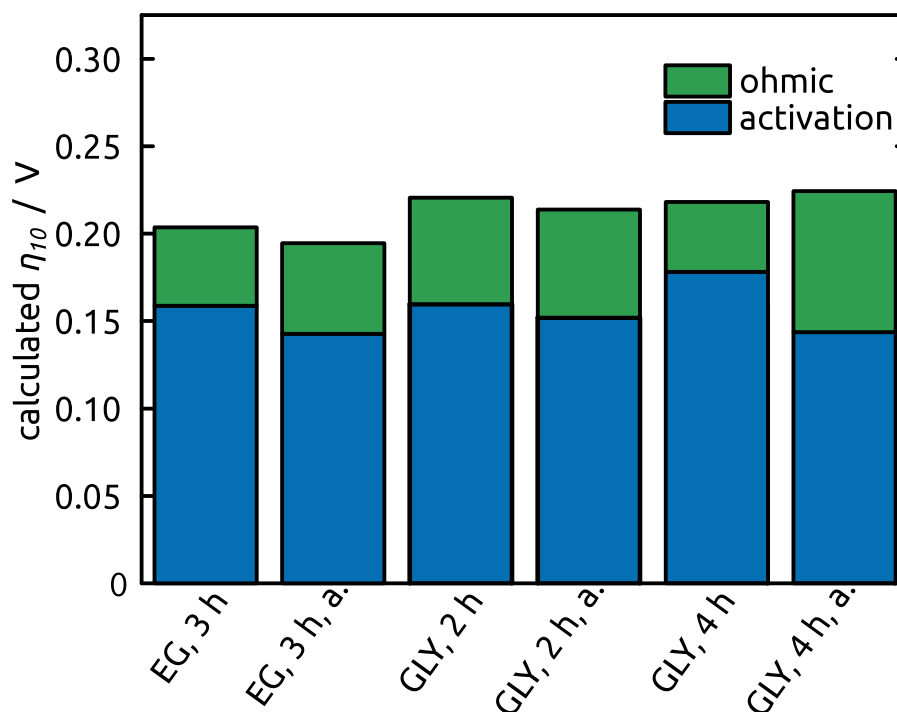
Fig. 4. Calculation of the activation and ohmic overpotential values required to yield a current density of 10 mA cm^{-2} by fitting linear sweep voltammety (scan rate 20 mV min^{-1}) of Ti6Al4V electrodes anodized in glycerol (2 h/4 h) or ethylene glycol (3 h) electrolytes and coated with Ir by ALD. Electrodes and electrolyte as in Fig. 3.

1 Ω cm^2, whereas electrodes in the anatase crystal structure are higher independently of the electrolyte or anodization duration. These results are in line with the steady-state electrolyses presented above, as well as with more dynamic measurements via cyclic voltammetry (CV, scan rate 50 mV s^{-1}). In CVs (Table 4), the amorphous samples yield higher current densities j_{max} at $\eta = 0.5$ V (EG: 65 mA cm^{-2}, GLY approx. 55 mA cm^{-2}) than the annealed ones (EG: 57 mA cm^{-2}, GLY approx. 45 mA cm^{-2}).

2.3. Stability

Besides performance, practical applicability also requires sufficient stability of electrodes in operating conditions. For this study, we will distinguish between chemical and electrochemical stability. The former is quantified by EDX and ICP and the latter by EIS and electrolyses.

a. Chemical stability

Corrosion of the scaffold and losses of noble metal catalyst can be investigated via analysis of the solid electrode (energy-dispersive X-ray microanalysis, EDX) and of the electrolyte (inductively coupled plasma coupled with mass spectrometry, ICP-MS). The comparison of atomic ratios between the electrodes' elements as quantified by EDX in the initial state (processed electrodes: anodized and Ir-coated) and after electrochemical characterization for a full duration of approx. 100 h (Supporting Information, Table S1) indicate minimal losses of Ir. A more sensitive method, ICP-MS enables us to track dissolved scaffold material (elements Ti, V) and catalyst (Ir) in the electrolyte (Table 5). Overall, losses of scaffold and catalyst material are correlated to one another. The most stable samples based on Ir values are the ones anodized in glycerol for 2 h.

b. Electrochemical stability

Is chemical stability reflected in stable electrochemical operation over several days? In order to compare samples of various performance levels in a fair manner, we submit them to electrolysis under a given current density ($j = 10$ mA cm^{-2}) and record the overpotential required to maintain it. A full picture of the various performance parameters and how they evolve with time is provided by repeating a cyclic procedure (shown in Supporting Information) that consists of galvanostatic electrolysis (1 h), chronoamperometric electrolyses at set overpotentials η=0.0 V to 0.5 V, and EIS characterization. These measurements are repeated in cycles for a total of 100 h (Fig. 6). The datapoints at $t = 0$ are delivered from the curves in Fig. 5 by interpolation. The overall increase of overpotentials with time reflects the slow degradation of the anodes. Annealed samples all degrade more significantly than their counterparts with no thermal treatment. As observed for the initial performance, the stability of electrodes in the latter group is identical within experimental uncertainties. The overpotential increases by 40 mV over 100 h (compare $\eta_{10,fnl.}$ and $\eta_{10,ini.}$ in Table 4).

The faster degradation and thus loss in performance of the annealed electrodes can be seen in the comparison of the initial and final Tafel plots (Fig. 5), showing a significant lower current density at the same overpotential (light blue, green and orange). The amorphous anodes maintain their performance.

Electrochemical impedance spectroscopy (EIS) enables the experimentalist to distinguish between various origins for an overall overpotential. Figure 7 summarizes the changes over 100 h in the most physically relevant quantities extracted from the fits. Neither of the two capacitances nor R_{por} (which is related to Ohmic losses along the pore length) exhibit significant trends. The charge transfer resistance R_{ct}, however, which is the direct quantification of electrocatalytic proficiency for the water oxidation, follows a trend that is perfectly parallel to that of η_{10}, Fig. 6. R_{ct} values all increase over time, slightly for amorphous electrodes and significant for previously annealed anodes.

Interestingly, there is no obvious correlation between the patterns observed for chemical stability (Table 5) and for electrochemical stability. Therefore, activity losses are not caused by dissolution of noble metal catalyst into the electrolyte. We conclude, then, that they must be related to the ripening of the catalytically active nanoparticles into larger ones and the concurrent loss in electrocatalytically active surface
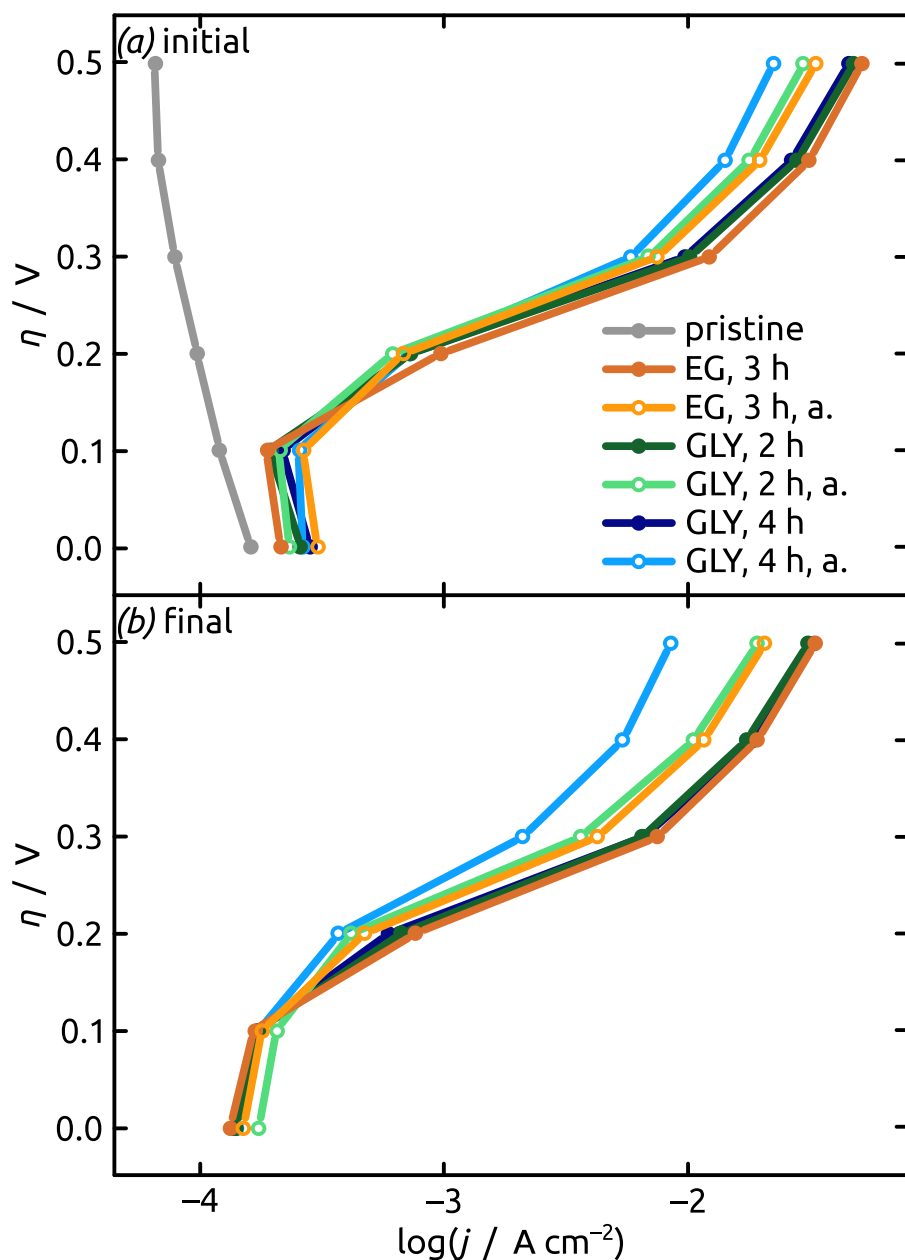
Fig. 5. Tafel plots of additive manufactured Ti6Al4V electrodes anodized in glycerol (2 h/4 h) or ethylene glycol (3 h) with optional annealing and Ir by ALD, as compared with a reference sample (pristine Ti6Al4V scaffold without anodization nor Ir coating). Chronoamperometry measurements were performed for 2 h each in the conditions described in Fig. 3. The value presented is the experimental current density averaged at each given overpotential over the second hour *(a)* initial and *(b)* final performance after 100 h of testing.

Table 4

Performance comparison of samples generated with different anodization parameters: left, steady-state electrochemical performance parameters (overpotential η_{10} required to reach 10 mA cm^{-2} initially/finally (after $\sim$ 100 h, as described in Figure 5)), middle: maximum current density j_{max} determined in CV (50 mV s^{-1}, η = 0.5 V) and right, charge transfer resistance R_{ct} determined by EIS (η = 0.4 V).

sample	$\eta_{10,ini.}$ V	$\eta_{10,fnl.}$ V	j_{max} mA cm^{-2}	R_{ct} Ω cm^2
EG, 3 h	0.29	0.33	65.2	0.66
EG, 3 h, a.	0.34	0.41	57.0	1.66
GLY, 2 h	0.30	0.34	58.3	1.13
GLY, 2 h, a.	0.34	0.40	42.4	1.26
GLY, 4 h	0.30	0.34	53.5	1.02
GLY, 4 h, a.	0.36	0.55	46.2	2.57

Table 5

ICP-MS analyses of electrolytes after $\sim$ 100 h of electrochemical performance measurements.

sample	Ti mg cm^{-2}	V mg cm^{-2}	Ir mg cm^{-2}
EG, 3 h	7.7	4.6	0.07
EG, 3 h, a.	15	5.4	0.09
GLY, 2 h	<1	<1	0.04
GLY, 2 h, a.	5.6	4.3	0.01
GLY, 4 h	14	4.4	0.10
GLY, 4 h, a.	<1	<1	0.03

area.

3. Conclusions

The results presented here establish the viability of a manufacturing procedure in which 3D printing of electrode scaffolds is used as a ver-
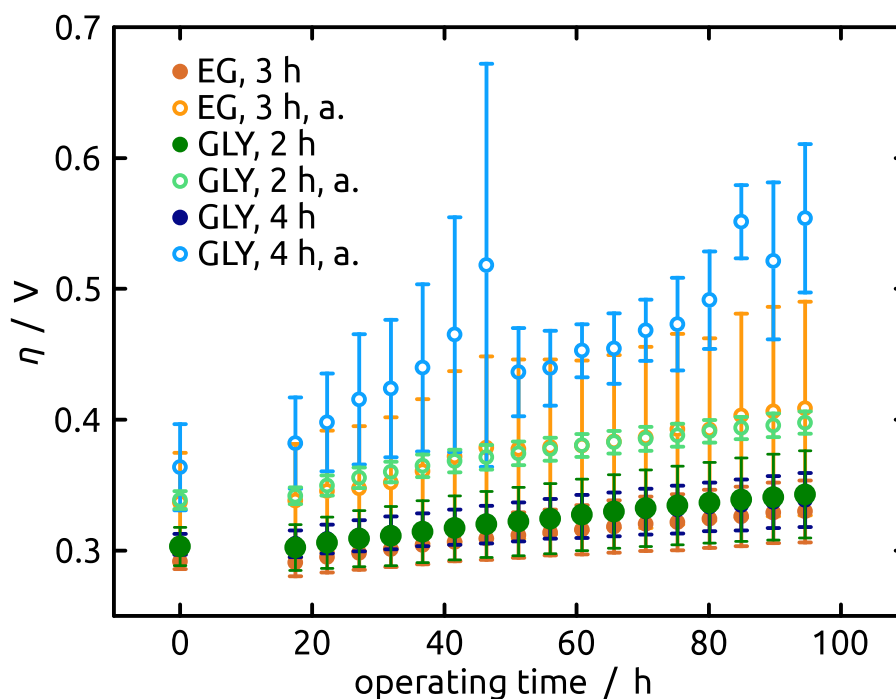
Fig. 6. Potentiometric measurements of η_{10} required to yield a current density of 10 mA cm^{-2} for 1 h of Ti6Al4V electrodes anodized in glycerol (2 h/4 h) or ethylene glycol (3 h) electrolytes and coated Ir by ALD. Other conditions as in Fig. 3.
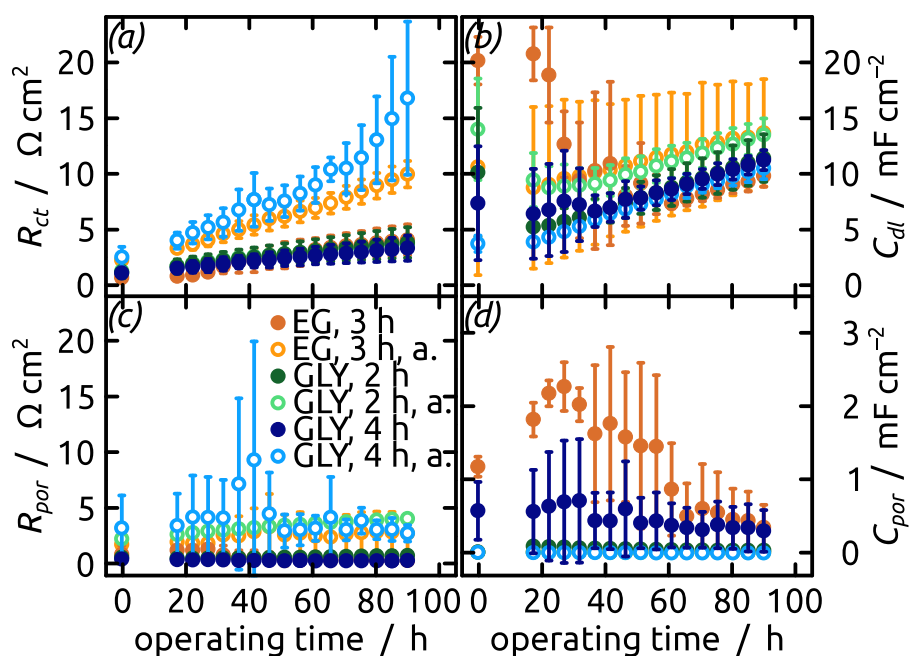

Fig. 7. EIS at $\eta = 0.4$ V of Ti6Al4V electrodes anodized in glycerol (2 h/4 h) or ethylene glycol (3 h) electrolytes and coated with Ir by ALD. Measurements were performed in 1 M H$_2$SO$_4$ at 60 °C using a three-electrode setup with a graphite auxiliary and (Hg/Hg$_2$SO$_4$/1 M H$_2$SO$_4$) reference electrode; presenting the progress of the resistance (R_{ct} and R_{por}) and capacitance (C_{dl} and C_{por}) within 100 h.

satile method of generating non-planar and highly controlled geometries, and combined with anodization and ALD to generate an electrocatalytically active surface of high area and efficient noble metal utilization. Specifically, the Ti6Al4V powder suitable for selective electron beam melting (SEBM) can be rendered stable in hot, concentric acid electrolyte using our methods. Importantly, low overpotentials can be achieved using minute amounts of iridium catalyst coating (<10 nm) in comparison with the μm thick coatings traditionally used in electrolysis cells.

Furthermore, the preparative methods used offer a variety of experimental parameters that can be varied in order to optimally adjust the electrodes to each application. We have characterized eight distinct quantitative values to characterize electrocatalytic performance and stability from various viewpoints. Figure 8 presents a comparison of all six electrode types with respect to these eight parameters (normalized on a scale of 0 to 1). The four parameters on the gray side characterize performance and include the electrochemically active surface area (*rf*), the mass activity of catalyst calculated from the maximum current
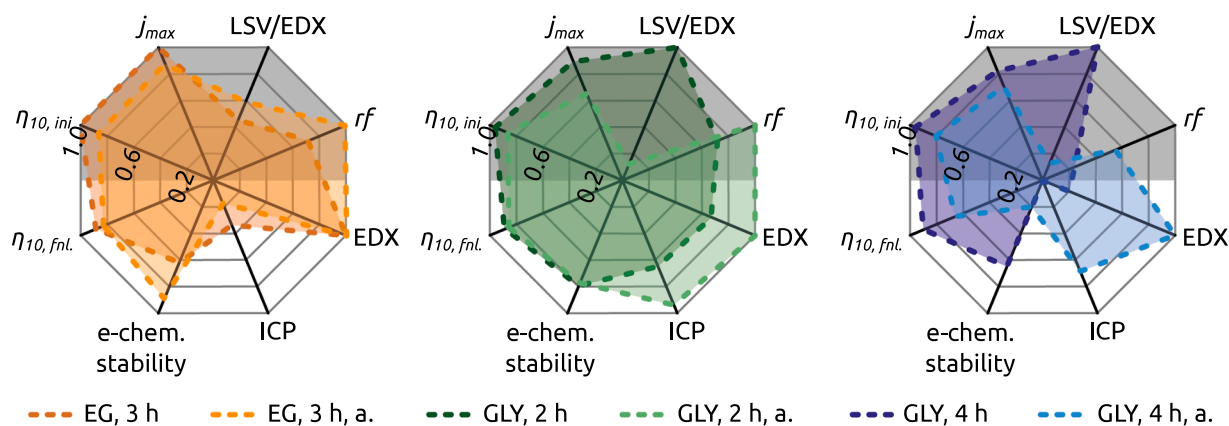
Fig. 8. Summary of performance (gray) and stability parameters quantified with eight distinct parameters for the six different types of samples compared here.

density with respect to EDX Ir quantification (LSV/EDX), the maximal current density achieved in CV (j_{max}), and the overpotential $\eta_{10,ini}$ initially required to reach 10 mA cm^{-2}. The four parameters on the white half represent stability in terms of overpotential $\eta_{10,fnl}$ after 100 h, the change in j_{max} after 100 h ('e-chem stability'), the losses of Ir in the electrolyte (ICP, the higher the losses the lower the value), and the change in EDX-determined Ir loading (EDX in Fig. 8). We highlight that all measurements and steady-state electrolyses have been performed in realistic operation conditions (1 M H$_2$SO$_4$, 60 °C, stirring).

The graphical representations provided in the Figure offer a holistic approach to choosing electrode types based on specific boundary conditions for applications. The highest current densities are achieved with the electrodes anodized in ethylene glycol, whereas the best performing electrode type overall (that is, considering noble metal utilization as well) is the one anodized for 2 h in glycerol without annealing. The latter type is in fact also the most balanced one if both performance and stability are considered. The most stable type is the one anodized in glycerol for 2 h and annealed.

4. Experimental

Materials

Standard chemicals (ammonium fluoride, ethylene glycol, glycerol, platinum wire) were purchased from Carl Roth and Alfa Aesar and used without further purification. Ethylcyclopentadienyl-iridium(I)-cyclohexa-1,3-diene ((EtCp)Ir(CHD)) was obtained from abcr and Ti6Al4V powder grade 23 from ECKART TLS, respectively.

Electrode fabrication

The cylindrical scaffolds were produced by means of electron beam powder bed fusion (E-PBF) using a Q10 Plus system (ARCAM AB, GE Additive, Mlndal Sweden). The material used was Ti6Al4V grade 23-powder with a particle size ranging between 45 μm and 105 μm. During the E-PBF process, a constant acceleration voltage of 60 kV was used, and a controlled helium pressure of $2 \cdot 10^{-3}$ mbar was set. The process cycle of E-PBF is divided into four process steps. First, a rake is used to apply the powder on the build plate, and then a defocused electron beam slightly preheats the powder layer. Subsequently, an equally defocused electron beam selectively sinters the powder particles according to the sliced CAD file. In the final step, the build plate is then lowered by a layer thickness ℓ_z of 50 μm, and the next powder layer is applied. This process cycle is repeated layer by layer until the component is completely built up. A more detailed description and further information about E-PBF can be found in a published article [16]. For the scanning pattern, an alternating xy raster with a line offset h$_s$ of 0.2 mm was chosen. The scan pattern was rotated by 90° after each layer ℓ_z. The samples were fabricated using a beam power $P = 552$ W, a scan speed of 10.8 m s^{-1}, a focus offset of 44 mA and 15 beam passes per layer. The

parameters were maintained constant throughout the build process.

Electrode preparation

The additively manufactured, tubular Ti6Al4V scaffolds were anodized for a duration of 2 h or 4 h using 0.5 wt.% NH$_4$F in a glycerol electrolyte with a water content of 12 vol.% under an applied potential (power supply by Elektro Automatik, EA-PSI 5200-10A) of 40 V, or under 60 V in ethylene glycol with 20 vol.% H$_2$O and 0.3 wt.% NH$_4$F for 3 h, in a purpose-built two-electrode cell with the anode sandwiched between two graphite counter-electrodes. The electrolyte was circulated by a peristaltic pump (Masterflex I/P Digital Drive) through a PE-heat exchanger (ElringKlinger Kunststofftechnik) in order to keep it at room temperature. The temperature of the cooling circuit was set to 18 °C and controlled by a chiller (Fryka ULK 2002). Ti6Al4V tubes anodized in the glycerol based electrolyte were rinsed with ethanol and water, soaked in ethanol overnight and dried subsequently. Using ethylene glycol as the organic solvent, the electrodes were soaked in water for 10 min, subsequently sonicated in ethanol and water for 10 min each, followed by drying.

Catalyst deposition

The Ir film was deposited afterwards using ALD in a commercial Gemstar-XT-6 ALD reactor from Arradiance. (EtCp)Ir(CHD) heated to 90 °C and ozone, generated by an ozone generator model BMT 803N, were used as precursors, whereas the reaction chamber was maintained at 220 °C. The tubular electrode scaffolds were held horizontal in the chamber, hanging a few millimeters from the sample holder in order to ensure homogeneous coating all around. The samples' color turned to a homogeneous black. The nominal Ir thickness of 9 nm was determined on Si(100) wafers by spectroscopic ellipsometry with a SENPro from SENTECH. Previous work has demonstrated that nucleation inhibition causes the deposit to be in particulate form and the true loading in the porous titania system to be significantly lower than this nominal value recorded on a planar reference sample suggests [30].

Electrochemical studies

The electrochemical performance [34] and stability characterizations [49] were performed in a temperature-controlled three-electrode setup by Gamry (Jacketed Euro Cell) at 60 °C using a heater/circulator by Julabo. The cell was equipped with a Hg/Hg$_2$SO$_4$/1 M H$_2$SO$_4$ reference electrode (RE, Sensortechnik Meinsberg) with a standard redox potential of +0.61 V versus NHE and a graphite auxiliary electrode. Cyclic voltammetry (CV), linear sweep voltammetry (LSV), electrochemical impedance spectroscopy (EIS), and chronoamperometric/chronopotentiometric steady-state electrolyses were recorded in a standard solution of aqueous 1 M H$_2$SO$_4$ electrolyte using a Gamry Interface 1000 potentiostat. CV and LSV were recorded with a scan rate of 50 mV s^{-1} and 20 mV min^{-1}, respectively, starting at the open circuit potential (OCP) between 0.0 V and +1.12 V. The applied potential for steady-state electrolyses was varied between +0.62 V and

+1.12 V vs. RE in steps of 0.1 V for 2 h each (overpotential range $\eta = 0.0$ V to 0.5 V). The current value averaged over the last hour of electrolysis are reported in the Tafel plot. EIS were recorded with the DC potential for each overpotential of the steady-state electrolysis in a frequency range of 100 kHz to 0.05 Hz and an AC voltage of 10 mV. A current density of 10 mA cm^{-2} was maintained for 1 h in chronopotentiometric electrolyses. The full program of electrochemical characterization is presented in Supporting Information.

Electrochemically active surface area determination

The electrochemically active surface area (ECSA) was determined by EIS using the same setup as for the electrochemical investigations described above. EIS were recorded with the DC potential -0.275 V vs. RE in the frequency range 100 kHz – 0.05 Hz and with an AC voltage of 10 mV.

Conductivity characterization

The anodized (and optionally annealed) Ti6Al4V scaffolds were pressed between two freshly polished Cu contacts by applying a weight of 2 kg for the conductivity characterizations. The voltage drop over the entire sample is measured using a voltmeter Agilent 34450 A and current meter Agilent 34410 A by applying a current of 1 A with a power supply EA-PSI 8016-20 T LCD. This measurement is repeated three times, whereas the same sample is removed and inserted again for each new measurement. The length of identical samples is varied (approx. 8, 5, 3 and 2 cm), whereas the edges of the samples are ground flat.

Analyses

The geometry, morphology and EDX mapping of the sintered Ti6Al4V and of the anodized and Ir-coated electrodes were investigated using a JSM-F100 field-emission scanning electron microscope by JEOL, the composition by a scanning electron microscope JEOL JSM 6400 equipped with a LaB$_6$ cathode combined with an energy-dispersive X-ray (EDX) detector from SAMx. The cross-section was prepared using an ion-beam cross-section polisher IB-19530CP by JEOL at an applied potential of 8.0 kV in an Ar flow of 4.5 sccm. The crystal structure was analyzed by X-ray diffraction (XRD) in Bragg-Brentano geometry using a Bruker D8 Advance equipped with a Cu Kα source and LynxEye XE detector.

The amount of Ir, Ti and V dissolved in the electrolyte after electrochemical characterization was determined by inductively coupled plasma mass spectrometry (ICP-MS, iCAP QC Thermo Scientific). For this analysis, calibrations (Ti: 305-6 µg L^{-1}, V: 59-3 µg L^{-1}, and Ir: 10-0.01 µg L^{-1}) were performed by diluting certified standards.

CRediT authorship contribution statement

André Hofer: Conceptualization, Methodology, Investigation, Visualization, Writing – original draft. **Sebastian Wachter:** Investigation. **Dirk Döhler:** Investigation. **Armin Laube:** Investigation. **Beatriz Sánchez Batalla:** Investigation. **Zongwen Fu:** Validation, Supervision. **Claudia Weidlich:** Validation, Resources. **Thorsten Struckmann:** Validation, Resources. **Carolin Körner:** Resources, Supervision, Funding acquisition. **Julien Bachmann:** Conceptualization, Validation, Resources, Writing – review & editing, Supervision, Project administration, Funding acquisition.

Declaration of Competing Interest

There are no conflicts to declare.

Acknowledgements

Supplementary material

Supplementary material associated with this article can be found, in the online version, at doi:10.1016/j.electacta.2022.140308.

References

[1] BMWi, Die nationale wasserstoffstrategie, Bundesministerium für Wirtschaft und Energie (BMWi), 2020.

[2] USDept.Energy, Hydrogen Program, U.S. Department of Energy, 2021.

[3] M. Pourbaix, Atlas of Electrochemical Equilibria in Aqueous Solutions, National Association of Corrosion Engineers, Houston, Texas, USA, 1974.

[4] D. Prando, A. Brenna, M.V. Diamanti, S. Beretta, F. Bolzoni, M. Ormellese, M. Pedeferri, Corrosion of titanium: Part 1: aggressive environments and main forms of degradation, J. Appl. Biomater. Funct. Mater. 15 (4) (2017) e291–e302, https://doi.org/10.5301/jabfm.5000387.

[5] N. Eliaz, Corrosion of metallic biomaterials: a review, Materials 12 (3) (2019) 407, https://doi.org/10.3390/ma12030407.

[6] C.R. Pobel, F. Osmanlic, M.A. Lodes, S. Wachter, C. Körner, Processing windows for Ti6Al4V fabricated by selective electron beam melting with improved beam focus and different scan line spacings, Rapid Prototyp. J. 25 (4) (2019) 665–671, https://doi.org/10.1108/RPJ-04-2018-0084.

[7] P. Heinl, A. Rottmair, C. Körner, R.F. Singer, Cellular titanium by selective electron beam melting, Adv. Eng. Mater. 9 (5) (2007) 360–364, https://doi.org/10.1002/adem.200700025.

[8] T. Scharowsky, A. Bauereiß, C. Körner, Influence of the hatching strategy on consolidation during selective electron beam melting of Ti6Al4V, Int. J. Adv. Manuf. Technol. 92 (5–8) (2017) 2809–2818, https://doi.org/10.1007/s00170-017-0375-1.

[9] L. Facchini, E. Magalini, P. Robotti, A. Molinari, Microstructure and mechanical properties of Ti6Al4V produced by electron beam melting of pre-alloyed powders, Rapid Prototyp. J. 15 (3) (2009) 171–178, https://doi.org/10.1108/13552540910960262.

[10] X. Xu, C. Li, J.G. Lim, Y. Wang, A. Ong, X. Li, E. Peng, J. Ding, Hierarchical design of NiOOH@Amorphous Ni-P bilayer on a 3D mesh substrate for high-efficiency oxygen evolution reaction, ACS Appl. Mater. Interfaces 10 (36) (2018) 30273–30282, https://doi.org/10.1021/acsami.8b06730.PMID: 30117733

[11] J.C. Bui, J.T. Davis, D.V. Esposito, 3D-printed electrodes for membraneless water electrolysis, Sustain. Energy Fuels 4 (2020) 213–225, https://doi.org/10.1039/C9SE00710E.

[12] M.P. Browne, J. Dodwell, F. Novotny, S. Jaśkaniec, P.R. Shearing, V. Nicolosi, D.J.L. Brett, M. Pumera, Oxygen evolution catalysts under proton exchange membrane conditions in a conventional three electrode cell vs. electrolyser device: a comparison study and a 3D-printed electrolyser for academic labs, J. Mater. Chem. A 9 (2021) 9113–9123, https://doi.org/10.1039/D1TA00633A.

[13] P.L. dos Santos, S.J. Rowley-Neale, A.G.-M. Ferrari, J.A. Bonacin, C.E. Banks, Ni-Fe (oxy)hydroxide modified graphene additive manufactured (3D-printed) electrochemical platforms as an efficient electrocatalyst for the oxygen evolution reaction, ChemElectroChem 6 (22) (2019) 5633–5641, https://doi.org/10.1002/celc.201901541.

[14] C.-Y. Lee, A.C. Taylor, S. Beirne, G.G. Wallace, A 3D-printed electrochemical water splitting cell, Adv. Mater. Technol. 4 (10) (2019) 1900433, https://doi.org/10.1002/admt.201900433.

[15] H. Sopha, A. Kashimbetova, L. Hromadko, I. Saldan, L. Celko, E.B. Montufar, J.M. Macak, Anodic TiO$_2$ nanotubes on 3D-printed titanium meshes for photocatalytic applications, Nano Lett. 0 (0) (2021) null, https://doi.org/10.1021/acs.nanolett.1c02815.PMID: 34609883

[16] C. Körner, Additive manufacturing of metallic components by selective electron beam melting a review, Int. Mater. Rev. 61 (5) (2016) 361–377, https://doi.org/10.1080/09506608.2016.1176289.

[17] K. Indira, U.K. Mudali, T. Nishimura, N. Rajendran, A review on TiO$_2$ nanotubes: influence of anodization parameters, formation mechanism, properties, corrosion behavior, and biomedical applications, J. Bio. Tribocorros. 1 (4) (2015) 28, https://doi.org/10.1007/s40735-015-0024-x.

[18] H. Fraoucene, V.A. Sugiawati, D. Hatem, M.S. Belkaid, F. Vacandio, M. Eyraud, M. Pasquinelli, T. Djenizian, Optical and electrochemical properties of self-organized TiO$_2$ nanotube arrays from anodized Ti6Al4V alloy, Front. Chem. 7 (2019) 66, https://doi.org/10.3389/fchem.2019.00066.

[19] S.B. Patel, A. Hamlekhan, D. Royhman, A. Butt, J. Yuan, T. Shokuhfar, C. Sukotjo, M.T. Mathew, G. Jursich, C.G. Takoudis, Enhancing surface characteristics of Ti6Al4V for bio-implants using integrated anodization and thermal oxidation, J. Mater. Chem. B 2 (23) (2014) 3597–3608, https://doi.org/10.1039/C3TB21731K.

[20] J.M. Macak, H. Tsuchiya, L. Taveira, A. Ghicov, P. Schmuki, Self-organized nanotubular oxide layers on Ti6Al7Nb and Ti6Al4V formed by anodization in NH$_4$F solutions, J. Biomed. Mater. Res. A 75 (4) (2005) 928–933, https://doi.org/10.1002/jbm.30501.

[21] R.L. Puurunen, Surface chemistry of atomic layer deposition: a case study for the trimethylaluminum/water process, J. Appl. Phys. 97 (12) (2005) 121301, https://doi.org/10.1063/1.1940727.

[22] H. Yang, R.Z. Waldman, Z. Chen, S.B. Darling, Atomic layer deposition for membrane interface engineering, Nanoscale 10 (44) (2018) 20505–20513.

[23] C. Detavernier, J. Dendooven, S. Pulinthanathu Sree, K.F. Ludwig, J.A. Martens, Tailoring nanoporous materials by atomic layer deposition, Chem. Soc. Rev. 40 (11) (2011) 5242–5253.

[24] P. Chen, T. Mitsui, D.B. Farmer, J. Golovchenko, R.G. Gordon, D. Branton, Atomic layer deposition to fine-tune the surface properties and diameters of fabricated nanopores, Nano Let. 4 (7) (2004) 1333–1337.

[25] J.W. Elam, D. Routkevitch, P.P. Mardilovich, S.M. George, Conformal coating on ultrahigh-aspect-ratio nanopores of anodic alumina by atomic layer deposition, Chem. Mater. 15 (18) (2003) 3507–3517.

[26] S.M. George, Atomic layer deposition: an overview, Chem. Rev. 110 (1) (2010) 111–131, https://doi.org/10.1021/cr900056b.

[27] J. Bachmann, Atomic layer deposition, a unique method for the preparation of energy conversion devices, Beilstein J. Nanotechnol. 4 (2014) 248–254, https://doi.org/10.3762/bjnano.5.26.

[28] S. Schlicht, M.K.S. Barr, M. Wu, P. Hoppe, E. Spiecker, W. Peukert, J. Bachmann, Minimization of catalyst loading on regenerative fuel cell positive electrodes based on titanium felts using atomic layer deposition, ChemElectroChem 5 (24) (2018) 3932–3937, https://doi.org/10.1002/celc.201801220.

[29] S. Schlicht, S. Haschke, V. Mikhailovskii, A. Manshina, J. Bachmann, Highly reversible water oxidation at ordered nanoporous iridium electrodes based on an original atomic layer deposition, ChemElectroChem 5 (9) (2018) 1259–1264, https://doi.org/10.1002/celc.201800152.

[30] S. Schlicht, P. Büttner, J. Bachmann, Highly active Ir/TiO2 electrodes for the oxygen evolution reaction using atomic layer deposition on ordered porous substrates, ACS Appl. Energy Mater. 2 (3) (2019) 2344–2349.

[31] S. Schlicht, K. Percin, S. Kriescher, A. Hofer, C. Weidlich, M. Wessling, J. Bachmann, Atomic layer deposition for efficient oxygen evolution reaction at Pt/Ir catalyst layers, Beilstein J. Nanotechnol. 11 (2020) 952–959, https://doi.org/10.3762/bjnano.11.79.

[32] S. Trasatti, Electrocatalysis in the anodic evolution of oxygen and chlorine, Electrochim. Acta 29 (11) (1984) 1503–1512, https://doi.org/10.1016/0013-4686(84)85004-5.

[33] S. Geiger, O. Kasian, B.R. Shrestha, A.M. Mingers, K.J.J. Mayrhofer, S. Cherevko, Activity and stability of electrochemically and thermally treated iridium for the oxygen evolution reaction, J. Electrochem. Soc. 163 (11) (2016) F3132–F3138, https://doi.org/10.1149/2.0181611jes.

[34] A. Hofer, S. Bochmann, J. Bachmann, Properties, performance and stability of iridium-coated water oxidation electrodes based on anodized titanium felts, Sustain. Energy Fuels 5 (2021) 478–485, https://doi.org/10.1039/D0SE01577F.

[35] P. Roy, S. Berger, P. Schmuki, TiO2 nanotubes: synthesis and applications, Angew. Chem. Int. Ed. 50 (13) (2011) 2904–2939, https://doi.org/10.1002/anie.201001374.

[36] H. Tsuchiya, P. Schmuki, Less known facts and findings about TiO2 nanotubes, Nanoscale 12 (2020) 8119–8132, https://doi.org/10.1039/D0NR00367K.

[37] J.M. Macak, H. Tsuchiya, L. Taveira, S. Aldabergerova, P. Schmuki, Smooth anodic TiO2 nanotubes, Angew. Chem. Int. Ed. 44 (45) (2005) 7463–7465, https://doi.org/10.1002/anie.200502781.

[38] J.M. Mack, H. Tsuchiya, P. Schmuki, High-aspect-ratio TiO2 nanotubes by anodization of titanium, Angew. Chem. Int. Ed. 44 (14) (2005) 2100–2102, https://doi.org/10.1002/anie.200462459.

[39] J. Hämäläinen, M. Kemell, F. Munnik, U. Kreissig, M. Ritala, M. Leskelä, Atomic layer deposition of iridium oxide thin films from Ir(acac)3 and ozone, Chem. Mat. 20 (9) (2008) 2903–2907, https://doi.org/10.1021/cm7030224.

[40] T. Aaltonen, M. Ritala, V. Sammelselg, M. Leskelä, Atomic layer deposition of iridium thin films, J. Electrochem. Soc. 151 (8) (2004) G489–G492, https://doi.org/10.1149/1.1761011.

[41] P. Fonda, Z. Wang, K. Yamazaki, Y. Akutsu, A fundamental study on Ti6Al4V's thermal and electrical properties and their relation to EDM productivity, J. Mater. Process. Technol. 202 (1–3) (2008) 583–589, https://doi.org/10.1016/j.jmatprotec.2007.09.060.

[42] L. Bolzoni, E.M. Ruiz-Navas, E. Gordo, Flexural properties, thermal conductivity and electrical resistivity of prealloyed and master alloy addition powder metallurgy Ti6Al4V, Mater. Des. 52 (2013) 888–895, https://doi.org/10.1016/j.matdes.2013.06.036.

[43] G. Li, L. Anderson, Y. Chen, M. Pan, P.-Y. Abel Chuang, New insights into evaluating catalyst activity and stability for oxygen evolution reactions in alkaline media, Sustain. Energy Fuels 2 (1) (2018) 237–251, https://doi.org/10.1039/c7se00337d.

[44] S. Watzele, A.S. Bandarenka, Quick determination of electroactive surface area of some oxide electrode materials, Electroanalysis 28 (10) (2016) 2394–2399, https://doi.org/10.1002/elan.201600178.

[45] M. Łukaszewski, M. Soszko, A. Czerwiński, Electrochemical methods of real surface area determination of noble metal electrodes – an overview, Int. J. Electrochem. Sci. 11 (2016) 4442–4469.

[46] D. Falcão, A. Pinto, A review on PEM electrolyzer modelling: guidelines for beginners, J. Clean. Prod. 261 (2020) 121184, https://doi.org/10.1016/j.jclepro.2020.121184.

[47] A. Angulo, P. van der Linde, H. Gardeniers, M. Modestino, D. Fernndez Rivas, Influence of bubbles on the energy conversion efficiency of electrochemical reactors, Joule 4 (3) (2020) 555–579, https://doi.org/10.1016/j.joule.2020.01.005.

[48] A. Laube, A. Hofer, S. Ressel, A. Chica, J. Bachmann, T. Struckmann, Pem water electrolysis cells with catalyst coating by atomic layer deposition, Int. J. Hydrog. Energy 46 (79) (2021) 38972–38982, https://doi.org/10.1016/j.ijhydene.2021.09.153.

[49] M. Suermann, B. Bensmann, R. Hanke-Rauschenbach, Degradation of proton exchange membrane (PEM) water electrolysis cells: looking beyond the cell voltage increase, J. Electrochem. Soc. 166 (10) (2019) F645–F652, https://doi.org/10.1149/2.1451910jes.